



Cite this: *RSC Adv.*, 2023, 13, 638

# Effective reduction of nitric oxide over a core–shell Cu–SAPO-34@Fe–MOR zeolite catalyst†

Xu Ting-ting,<sup>a</sup> Li Gang-gang,<sup>b</sup> Zheng Kai-hua,<sup>a</sup> Zhang Xin-yan,<sup>a</sup> \*<sup>ad</sup> Zhang Xin\*<sup>a</sup> and Zhang Shao-qing<sup>c</sup>

In this study, a core–shell catalyst of Cu–SAPO-34@Fe–MOR was successfully prepared through a silica-sol adhesion method, and its performance for selective catalytic reduction of nitric oxide by NH<sub>3</sub> (NH<sub>3</sub>-SCR) was evaluated in detail. The Fe–MOR coating has not only increased the high-temperature activity and broadened the reaction temperature window of Cu–SAPO-34 to a large extent, but also increased the hydrothermal stability of Cu–SAPO-34 markedly. It is demonstrated that a strong synergistic interaction effect exists between Cu<sup>2+</sup> and Fe<sup>3+</sup> ions and promotes the redox cycle and oxidation–reduction ability of copper ions, which greatly accelerates the catalytic performance of the core–shell Cu–SAPO-34@Fe–MOR catalyst. Abundant isolated Cu<sup>2+</sup> ions and Fe<sup>3+</sup> ions on the ion exchange sites performing NO<sub>x</sub> reduction at low and high temperature region lead to the broad reaction temperature window of Cu–SAPO-34@Fe–MOR. In addition, more weakly adsorbed NO<sub>x</sub> species formed and the increased number of Lewis acid sites may also contribute to the higher catalytic performance of Cu–SAPO-34@Fe–MOR. On the other hand, the better hydrothermal ageing stability of Cu–SAPO-34@Fe–MOR is related to its lighter structural collapse, fewer acidic sites lost, more active components (Cu<sup>2+</sup> and Fe<sup>3+</sup>) maintained, and more monodentate nitrate species formed in the core–shell catalyst after hydrothermal ageing. Last, the mechanism study has found that both Langmuir–Hinshelwood (“L–H”) and Eley–Rideal (“E–R”) mechanisms play an essential role in the catalytic process of Cu–SAPO-34@Fe–MOR, and constitute another reason for its higher activity compared with that of Cu–SAPO-34 (only “L–H” mechanism).

Received 24th October 2022  
Accepted 15th December 2022

DOI: 10.1039/d2ra06708k

rsc.li/rsc-advances

## 1. Introduction

NH<sub>3</sub>-SCR technology has been widely found to be one of the most effective methods for purifying nitrogen oxide (NO<sub>x</sub>) pollutants in diesel vehicle exhaust gases.<sup>1</sup> Among various NH<sub>3</sub>-SCR catalysts, transition metal loaded zeolite catalysts have attracted the most attention because of their excellent catalytic activities and large specific surface areas.<sup>2,3</sup> Significantly, the Cu and Fe ion-exchanged zeolites have high application value for removing NO<sub>x</sub> by NH<sub>3</sub>-SCR reaction. However, they each have certain limitations of their own. On the one hand, the Cu zeolite catalyst has good low-temperature activity and N<sub>2</sub> selectivity in

the denitrification process, but its high-temperature activity is not satisfactory, and its hydrothermal stability needs to be improved. On the other hand, the Fe zeolite catalyst has better high-temperature activity and hydrothermal stability, but its low-temperature activity is poor, resulting in a confined reaction temperature range. Hence, to meet industrial applications, researchers have prepared bimetal-exchanged zeolite (Cu and Fe) catalysts by combining their respective advantages, which has proved to be a feasible strategy.<sup>4,5</sup> For example, the Fe–Cu-beta catalyst was prepared by two-step ion exchange method, and it not only maintains the low-temperature activity of Cu-beta zeolites, but also improves its high-temperature activity and widens the temperature window.<sup>4</sup> Coincidentally, Zhao *et al.*<sup>5</sup> used a liquid-phase ion exchange method to load Fe on Cu-CHA, and the bimetallic zeolites catalyst presented increased low-temperature activity and a wider temperature window. The above researches have revealed that there is strong synergy effect between Cu and Fe species on Cu–Fe bimetallic zeolites and both the active sites and the oxidation–reduction ability of the catalyst have changed, which may lead to the combination of their catalytic advantages and result in more excellent low temperature activity and improved temperature window. However, the current researches on Cu–Fe bimetallic zeolites are still very preliminary, for example, the mechanism

<sup>a</sup>School of Chemistry and Environmental Engineering, Changchun University of Science and Technology, Changchun 130022, P. R. China. E-mail: zhangxinyan@cust.edu.cn; zhangxin06@cust.edu.cn; Fax: +86-431-8558-3152; Tel: +86-431-8558-3152

<sup>b</sup>National Engineering Laboratory for VOCs Pollution Control Material & Technology, University of Chinese Academy of Sciences, Beijing 101408, P. R. China

<sup>c</sup>Key Laboratory of Wetland Ecology and Environment, Northeast Institute of Geography and Agroecology, Chinese Academy of Sciences, 4888 Shengbei Street, North District of Changchun High, Changchun, Jilin 130102, China

<sup>d</sup>Chongqing Research Institute, Changchun University of Science and Technology, Chongqing 401135, P. R. China

† Electronic supplementary information (ESI) available. See DOI: <https://doi.org/10.1039/d2ra06708k>



of the interaction between Cu and Fe is not precise, and their activities and temperature window need to be further improved to meet the application needs.

Recently, fabricating core-shell morphology catalysts has gained special attention from researchers due to their unique structure and potential broad application value.<sup>6–8</sup> A variety of zeolites materials with core-shell structure (zeolites@zeolites) have been prepared. It is found the particular core-shell structure not only achieved extra synergistic effects between the core and shell part and combined their advantages, but also the special shell structure could act as a certain protective effect or layer on the active center of the inner core.<sup>9–12</sup> Du *et al.*<sup>11</sup> successfully prepared core-shell Fe-ZSM-5@Silicalite-1 catalyst by secondary hydrothermal crystallization method, and its catalytic performance for NH<sub>3</sub>-SCR has been significantly improved, which may be due to the combining the advantages of the two zeolites and the realization of functional complementarity. Chen *et al.*<sup>12</sup> have found that the coating of ZSM-5 on Cu-CHA could act as a hydrophobic layer and significantly increase its hydrothermal stability and water resistance. The above researches have indicated the special core-shell structure may achieve improved catalytic performance probably due to the synergistic effects between the core and shell part and the certain protective effect of the shell layer, resulting in great potential wide application and research value.<sup>13,14</sup> However, although the promising Cu-Fe bimetallic zeolites have been greatly concerned, till now the study of special core-shell Cu-Fe bimetallic zeolites has not been reported, which has greater opportunity to combine the supremacy of Cu and Fe zeolites to exhibit excellent catalytic performance in NH<sub>3</sub>-SCR.<sup>15</sup>

In this study, a core-shell catalyst of Cu-SAPO-34@Fe-MOR was successfully prepared through a simple silica-sol adhesion method, and its performance for selective catalytic reduction of nitric oxide by NH<sub>3</sub> (NH<sub>3</sub>-SCR) was evaluated in detail. A variety of characterization techniques were used to study the mechanism of Fe-MOR coating on Cu-SAPO-34 and their synthetic effect between core-shell layers systematically.

## 2. Experimental section

### 2.1 Catalyst preparation

Cu-SAPO-34 and Fe-MOR samples were prepared by ion-exchange of commercial SPAO-34 and MOR zeolites with 0.05 mol L<sup>−1</sup> Cu(NO<sub>3</sub>)<sub>2</sub>·3H<sub>2</sub>O and 0.05 mol L<sup>−1</sup> Fe(NO<sub>3</sub>)<sub>3</sub>·9H<sub>2</sub>O, respectively. The core-shell Cu-SAPO-34@Fe-MOR catalysis with Cu-SAPO-34 as the core and Fe-MOR as the shell was prepared by the physical combination method.<sup>15</sup> First, the Cu-SAPO-34 and Fe-MOR were ground into a fine powder with a particle size of about 90–120 μm. Then, Cu-SAPO-34 was immersed in a solution of 30% silica sol and deionized water for 30 minutes. The mixed system was poured into a flask containing a certain amount of Fe-MOR powder, and shook for 1 hour for uniform coating. Finally, the obtained sample was dried at 120 °C for 12 hours and then baked in a muffle furnace at 500 °C for 4 hours, and the obtained sample was denoted as Cu-SAPO-34@Fe-MOR. Five levels of concentration of silica sol (5%, 10%, 15%, 20% and 30%) were used to research the effect

of silica sol on the catalysts preparation and their reaction performances, and it was recorded as Cu-SAPO-34@Fe-MOR<sub>x</sub> (X represents the concentration of silica sol). Samples with different core-shell mass ratios were prepared and named as Cu-SAPO-34@Fe-MOR(*a*:*b*), where *a*:*b* represents the mass ratio of Cu-SAPO-34 (*a*) to Fe-MOR (*b*). Without special explanation, Cu-SAPO-34@Fe-MOR refers to the sample prepared with 10% concentration of silica sol and core-shell ratio of 1:2. The physical mixing of Cu-SAPO-34 and Fe-MOR is obtained by ultrasonic dispersion method.<sup>16</sup> Fe-MOR and Cu-SAPO-34 were dispersed in distilled water and sonicated for 30 minutes. The product was dried overnight and calcined at 550 °C for 4 hours to obtain the final sample, which is recorded as Cu-SAPO-34/Fe-MOR.

### 2.2 Catalyst characterization

The synthesized catalysts were systemically characterized by a variety of characterization methods. Detailed information and processes are disclosed in the ESI.†

### 2.3 NH<sub>3</sub>-SCR test

The NH<sub>3</sub>-SCR reaction activity test of the catalyst is carried out on a fixed-bed reactor. 200 mg of catalyst was added to a quartz tube with an inner diameter of 8 mm, and passed a simulated diesel vehicle exhaust with total flow of 500 mL min<sup>−1</sup>. The gas composition is 500 ppm NO, 500 ppm NO and 5% O<sub>2</sub> with N<sub>2</sub> as the balance gas. A flue gas analyzer (Thermo model 42i-HL) was used to measure the nitrogen oxides of the import and export gases. Data were recorded every 25 °C intervals from 150 °C to 550 °C.

The NO conversion of the catalyst is calculated according to the following eqn:

$$\text{NO conversion (\%)} = \frac{[\text{NO}]_{\text{in}} - [\text{NO}]_{\text{out}}}{[\text{NO}]_{\text{in}}} \times 100\%$$

where [NO]<sub>in</sub> and [NO]<sub>out</sub> are the molar flow rates of NO at the inlet and outlet of the reaction instrument.

### 2.4 Hydrothermal ageing performance test

The rapid hydrothermal ageing device in the laboratory was used to evaluate the hydrothermal stability of the catalyst. The test conditions are as follows: 10% H<sub>2</sub>O, N<sub>2</sub> as equilibrium gas, treatment at 750 °C for 12 hours. The sample after hydrothermal ageing is named as X-750, where X represents the fresh catalyst before ageing treatment.

## 3. Results and discussion

### 3.1 Exploration of material preparation conditions

**3.1.1 Effect of different silica sol concentrations.** The influence of preparation conditions, such as concentration of silica sol and core-shell mass ratio, on the activities of prepared catalysts was studied in details. Fig. 1 shows that the prepared material exhibits the best catalytic performance when the concentration of silica sol is 10% (Fig. 1a). The *T*<sub>50</sub> (the temperature where NO conversion rate reaches 50%) and *T*<sub>90</sub>



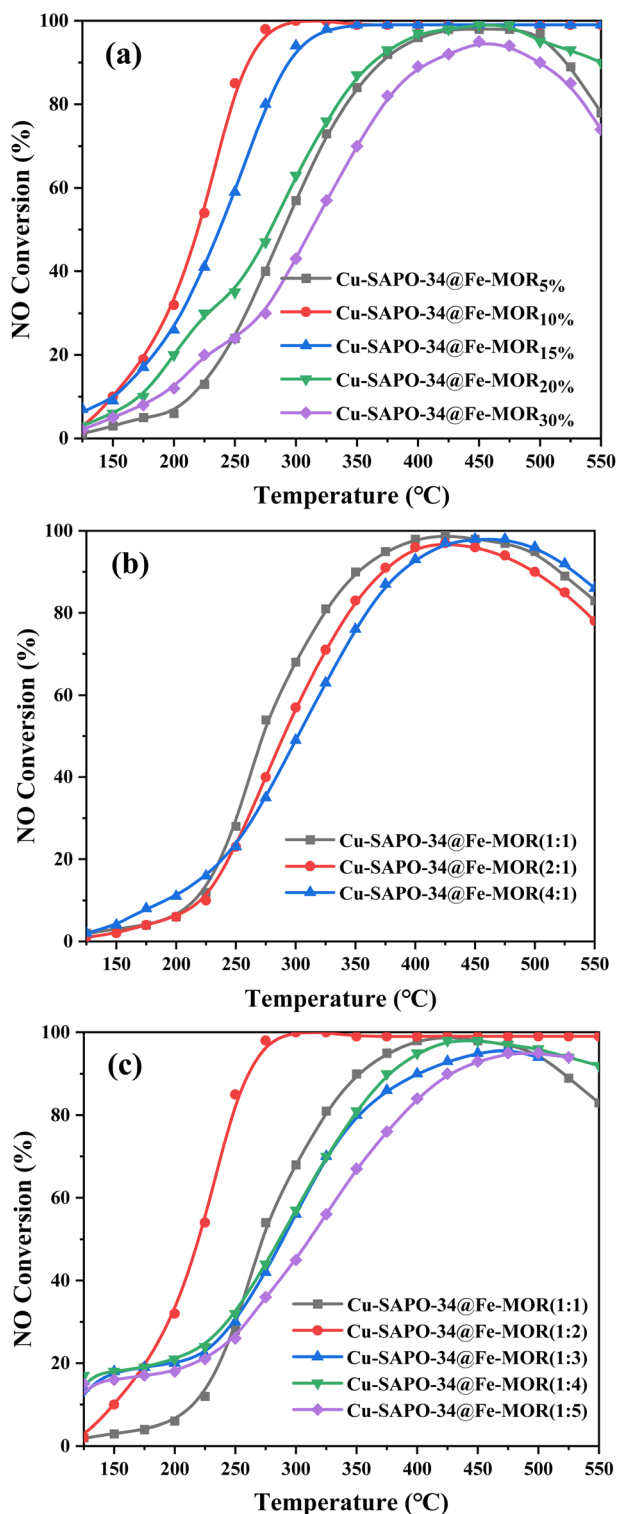


Fig. 1 NO conversion of Cu-SAPO-34@Fe-MOR samples prepared with different silica sol concentrations (a) NO conversion of Cu-SAPO-34@Fe-MOR samples prepared with different core-shell mass ratio:  $m_C : m_S > 1$  (b) and  $m_C : m_S > 1$  (c).

(the temperature where NO conversion rate reaches 90%) occur at 200 °C and 235 °C, respectively. Also, the  $DT_{90}$  (the temperature range where the NO conversion rate is above 90%) of Cu-

SAPO-34@Fe-MOR<sub>10%</sub> is the widest (235 °C–550 °C). However, when the concentration of silica sol is below 10% or above 10%, the NO conversion rate of the catalyst is reduced to varying degrees. This may be because silica sol is acting as a binder; lack of silica sol would cause worse bonding effect, and excess silica sol may cause Cu-SAPO-34 and Fe-MOR to agglomerate and cannot form a uniformly dispersed core-shell structure.

**3.1.2 Effect of different mass ratios on core-shell.** The results in Fig. 1b have shown that the core-shell mass ratio of the prepared materials has significant effect on their catalytic performance. When the core-shell ratio of the catalysts is above 1 ( $m_C : m_S > 1$ ), their NO conversion rates elevate with the increase of core-shell ratio, *i.e.* Fe-MOR dosage, but the reaction temperature window of all catalysts in this dosage range is relatively narrow. Among them, Cu-SAPO-34@Fe-MOR(1:1) exhibits the best catalytic performance with the  $DT_{90}$  of only 175 °C (350 °C–525 °C). The main reason is probably that the Fe-MOR amount is too few to completely coat the Cu-SAPO-34 zeolite to form a capsule shell. Therefore, the Fe-MOR amount is increased, and the core-shell mass ratio is changed to  $m_C : m_S < 1$ . It is found (Fig. 1c) that the core-shell catalyst with  $m_C : m_S = 1:2$  exhibits the best low temperature  $NH_3$ -SCR activity (reaches  $T_{90}$  at 225 °C) and the widest reaction temperature window ( $DT_{90}$  from 225 °C to 550 °C). The above results have shown that an appropriate amount of Fe-MOR or core-shell mass ratio of Cu-SAPO-34 to Fe-MOR is very important to the catalytic performance of the core-shell catalyst.

By exploring the preparation conditions, we have determined that the optimal amount of silica sol is 10%, and the optimal core-shell mass ratio is 1:2 ( $m_{Cu-SAPO-34} : m_{Fe-MOR}$ ) to prepare the core-shell Cu-SAPO-34@Fe-MOR catalysts. In the following work, we will study and analyze the catalyst on this basis, and without special instructions, the sample Cu-SAPO-34@Fe-MOR refers to a catalyst with a silica sol dosage of 10% and a core-shell mass ratio of 1:2 mentioned above.

## 3.2 $NH_3$ -SCR performance of Cu-SAPO-34@Fe-MOR

**3.2.1 Catalyst activity.** The catalytic activities of the prepared Cu and Fe zeolites materials for  $NH_3$ -SCR were evaluated, as shown in Fig. 2a. Cu-SAPO-34 exhibits good low-temperature activity but the activity decreases significantly above 350 °C. Fe-MOR exhibits quite good activity above 350 °C, but inferior activity at low-temperature. These results are consistent with the reports in the literature.<sup>17</sup> Fortunately, after Cu-SAPO-34 is coated with Fe-MOR, the reaction window of Cu-SAPO-34@Fe-MOR is significantly widened compared with Cu-SAPO-34 and Fe-MOR (as shown in Table 1), and the  $DT_{95}$  (the temperature range where the NO conversion rate is higher than 95%) of Cu-SAPO-34@Fe-MOR is increased to be 280 °C (from 270 °C to 550 °C). Not only the activity of Cu-SAPO-34@Fe-MOR at low temperature is closed to Cu-SAPO-34, but also the high-temperature activity is improved than that of Fe-MOR. The catalytic performance of the core-shell catalyst of Cu-SAPO-34@Fe-MOR is also much better than that of the physically mixed Cu-SAPO-34/Fe-MOR. The above results clearly indicate that Fe-MOR coating has broadened the reaction temperature

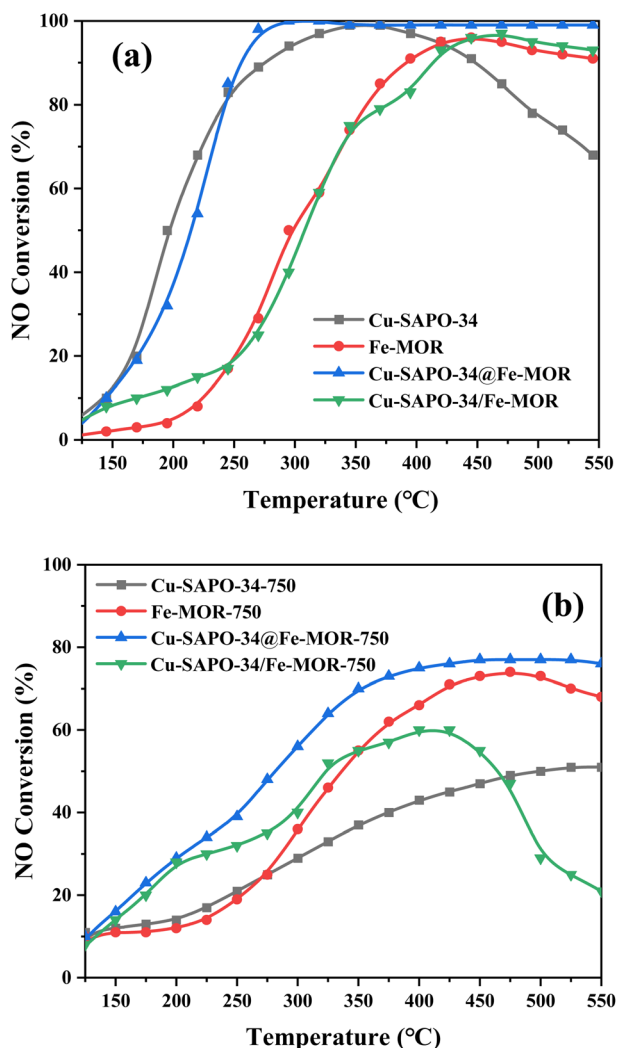


Fig. 2  $\text{NH}_3$ -SCR performance of fresh (a) and hydrothermal aging treated (b) Cu zeolites catalysts.

Table 1 The BET specific surface area and total pore volume of catalysts

Sample	BET surface areas ( $\text{m}^2 \text{g}^{-1}$ )	Total pore volume ( $\text{cm}^3 \text{g}^{-1}$ )
Cu-SAPO-34	453	0.274
Fe-MOR	265	0.207
Cu-SAPO-34@Fe-MOR	339	0.259
Cu-SAPO-34-750	415	0.217
Fe-MOR-750	253	0.201
Cu-SAPO-34@Fe-MOR-750	334	0.238

window of Cu-SAPO-34 to a large extent, and the core-shell Cu-SAPO-34@Fe-MOR catalyst has shown excellent catalytic performance and high potential application value.

**3.2.2 Hydrothermal stability.**  $\text{NO}_x$  removal from diesel vehicles exhaust should also consider the long-term hydrothermal stability of the catalysts. Therefore, we have conducted the test of hydrothermal aging performance. Fig. 2b shows the

$\text{NH}_3$ -SCR activities of the prepared Cu-SAPO-34 catalysts after hydrothermal ageing at  $750^\circ\text{C}$ . The activity of Cu-SAPO-34 decreases seriously after hydrothermal aging, while that of Fe-MOR maintains better. This result is similar to those reported in the literature.<sup>18,19</sup> After Fe-MOR coating, the activity of Cu-SAPO-34@Fe-MOR remains much better than Cu-SAPO-34, even better than Fe-MOR. In addition, core-shell Cu-SAPO-34@Fe-MOR catalyst also shows much better hydrothermal stability than physical mixed catalyst Cu-SAPO-34/Fe-MOR, which has lost its activity dramatically at high temperature (above  $425^\circ\text{C}$ ). The above results indicate that the coating of Fe-MOR may help enhance hydrothermal stability of the composite catalyst through making core-shell structure. This protection effect has ever been reported and is consistent with the findings of Chen *et al.*<sup>12</sup>

### 3.3 Characterization of Cu-SAPO-34@Fe-MOR catalysts

**3.3.1 XRD and BET results.** As shown in Fig. S1,<sup>†</sup> the XRD pattern of Cu-SAPO-34@Fe-MOR presents the characteristic peaks of both SAPO-34 and MOR, indicating the successful synthesis of composite sample.<sup>20</sup> In addition, no peaks related to oxides of Cu or Fe are observed, indicating that Cu and Fe species have good dispersibility on the composite samples. As shown in Fig. S2,<sup>†</sup> Cu-SAPO-34@Fe-MOR exhibits type I of  $\text{N}_2$  adsorption-desorption isotherms, indicating a typical microporous structure ( $<2 \text{ nm}$ ) is formed.<sup>21</sup> The BET specific surface area and total pore volume of Cu-SAPO-34, Fe-MOR and Cu-SAPO-34@Fe-MOR catalysts are shown in Table 1. Compared with Cu-SAPO-34, the BET specific surface area of Cu-SAPO-34@Fe-MOR has reduced by 25%, and the pore volume has decreased by 7%. This may be because Fe-MOR coated Cu-SAPO-34 and blocked a small amount of zeolites tunnel.

**3.3.2 SEM and TEM.** The macro morphology of the prepared catalysts is investigated by scanning electron microscope (SEM). Fig. 3A shows that Cu-SAPO-34 has a complete cubic structure with uniform particle size and a particle diameter of about  $2\text{--}3 \mu\text{m}$ , which is consistent with previous literature reports.<sup>22</sup> Fig. 3B shows that Fe-MOR is a composite formed by ribbon-shaped nanowires with a rough surface and uniform particle size distribution of about  $2\text{--}3 \mu\text{m}$ , and the morphological characteristics are also similar to the MOR reported in the literature.<sup>23</sup> Fig. 3C and D show that the morphology of Cu-SAPO-34@Fe-MOR exhibits basically an overall appearance of a cubic particle similar to that of Cu-SAPO-34, with an additional layer of nanowires similar to Fe-MOR attached on the surface. Combined with the results of SEM-mapping (Fig. 3E), it is found that Fe and Cu are uniformly dispersed in the catalyst, indicating the successful covering of Fe-MOR on the surface of the composite catalyst.

To further confirm the core-shell structure of Cu-SAPO-34@Fe-MOR, TEM images of Cu-SAPO-34@Fe-MOR are shown in Fig. 4. The results have revealed (Fig. 4A–C) that a layer of nanowire film is coated on the surface of the composite catalyst. Moreover, the line scan results (Fig. 4D) of the elements over Cu-SAPO-34@Fe-MOR have further confirmed that Fe-MOR is





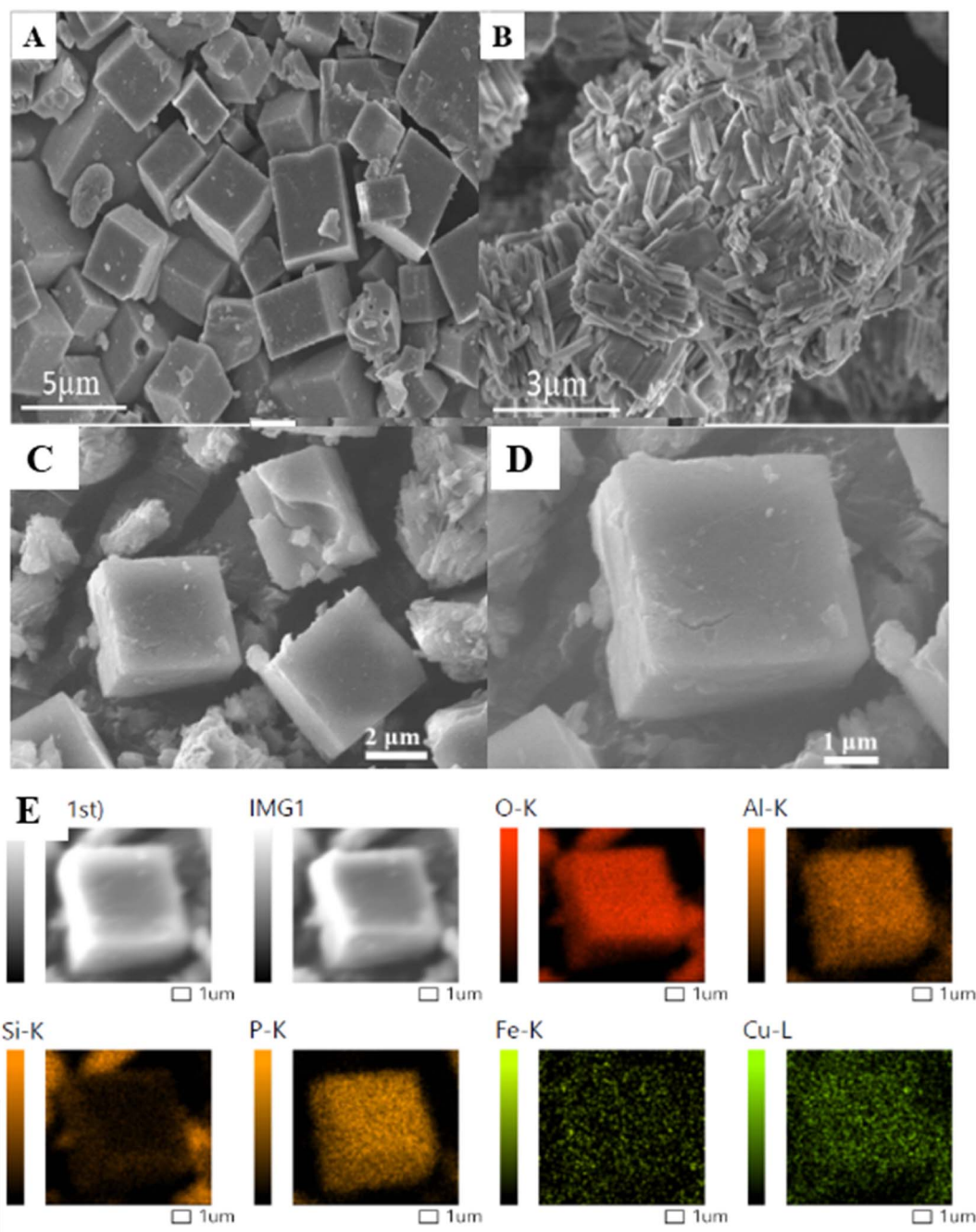


Fig. 3 SEM pictures of Cu-SAPO-34 (A), Fe-MOR (B) and Cu-SAPO-34@Fe-MOR (C and D); SEM-mapping of Cu-SAPO-34@Fe-MOR(E).

coating as a shell layer on the surface of Cu zeolites, based on elements distribution of the composite.

**3.3.3  $\text{NH}_3$ -TPD results.**  $\text{NH}_3$ -TPD is used to quantitatively analyze the acid sites of Cu-SAPO-34@Fe-MOR. As described in Fig. 5, three peaks are observed in Cu-SAPO-34. According to literature, the peaks in low-temperature region are caused by physically adsorbed  $\text{NH}_3$  or  $\text{NH}_3$  desorption at weak Lewis sites (peak  $\alpha$ ). The peak at about 300 °C is ascribed to  $\text{NH}_3$  desorption at the strong Lewis acid site (peak  $\beta$ ). The peak above 400 °C is caused by  $\text{NH}_4^+$  decomposition at the Brønsted acid site (peak  $\gamma$ ).<sup>24</sup> Cu-SAPO-34@Fe-MOR also showed three desorption peaks

similar to Cu-SAPO-34, indicating the presence of  $\text{NH}_3$  adsorbed by physical adsorption and weak Lewis site (50–150 °C),  $\text{NH}_3$  adsorbed on strong Lewis site (150–300 °C) and  $\text{NH}_3$  adsorbed on Brønsted acid site (300–450 °C). By comparison of the area of  $\text{NH}_3$  desorption peaks (Table 2), it can be found that after Fe-MOR coating, the weakly adsorbed  $\text{NH}_3$  (physically adsorbed  $\text{NH}_3$  and adsorbed  $\text{NH}_3$  at weak Lewis sites for peak  $\alpha$ ) and the strong adsorbed  $\text{NH}_3$  ( $\text{NH}_4^+$  at the Brønsted acid site for peak  $\gamma$ ) on Cu-SAPO-34@Fe-MOR catalyst are much lower after Fe-MOR coating. However, the adsorbed  $\text{NH}_3$  with medium strength ( $\text{NH}_3$  adsorbed on strong Lewis site for peak  $\beta$ ) is increased



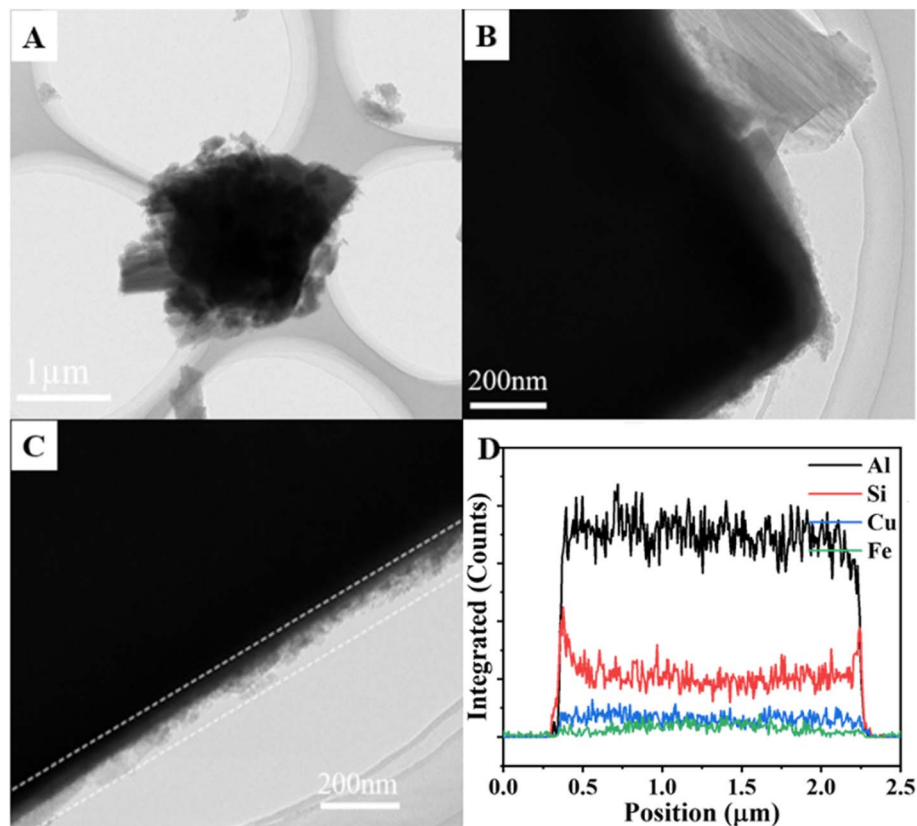


Fig. 4 TEM image (A–C) and the line scanning (D) of Cu-SAPO-34@Fe-MOR.

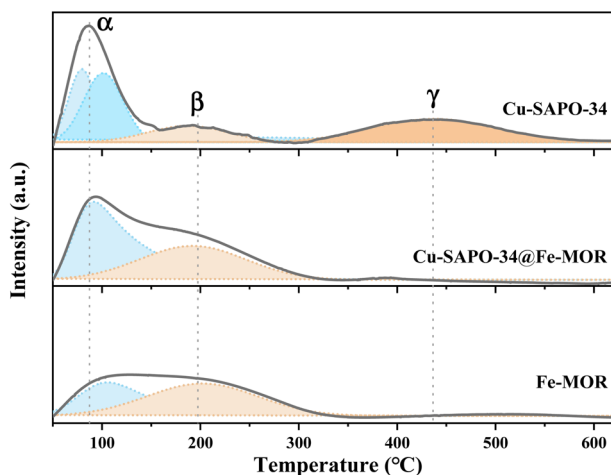


Fig. 5  $\text{NH}_3$ -TPD results of Cu-SAPO-34, Fe-MOR and Cu-SAPO-34@Fe-MOR.

significantly, which may have a good influence on the catalytic properties as reported by previous researches.<sup>11</sup>

**3.3.4 UV-vis DRS.** UV-vis spectroscopy is an effective method to characterize various copper species in the zeolites. By properly deconvolving the characteristic absorption bands of UV-vis DRS spectra (Fig. 6), different specific Cu and Fe species in the Cu-SAPO-34, Fe-MOR and Cu-SAPO-34@Fe-MOR catalysts are identified. There are generally three characteristic

absorption bands for copper species in copper-exchanged zeolite: the band at 218 nm is ascribed to the ligand to metal charge transfer of  $\text{Cu}^{2+}$  ion species, which is associated with ( $\text{O}^{2-}\text{Cu}^{2+} \rightarrow \text{O}^-\text{Cu}^+$ ),<sup>25</sup> the band at the 800 nm is ascribed to the d-d transitions in  $\text{Cu}^{2+}$  species, and the band at 400–600 nm is ascribed to the CuO oxide species, respectively.<sup>26,27</sup> Fig. 6 shows that  $\text{Cu}^{2+}$  ion is the dominant copper species in Cu-SAPO-34 catalyst. The UV-vis DRS results of Fe-MOR catalyst are consistent with previous researchers,<sup>28</sup> suggesting the existence of various Fe species in the ion exchange Fe-MOR zeolites. The primary bands at 215 nm and 285 nm indicate that isolated  $\text{Fe}^{3+}$  ions species is the dominant Fe species in Fe-MOR with small amount of iron oxide clusters in or iron oxide nanoparticles out the zeolite crystal channel. Cu-SAPO-34@Fe-MOR has quite similar UV-vis absorption with Cu-SAPO-34. The similar strong peak at around 220–280 nm and weak broadband at 300–400 nm indicate the existence of large amount of isolated  $\text{Cu}^{2+}$  and  $\text{Fe}^{3+}$  ions and a small number of copper oxide species, respectively. Also, the extra weak broad band above 600 nm suggests forming of a small amount of oligonuclear  $\text{Fe}^{3+}_x\text{O}_y$  clusters in Cu-SAPO-34@Fe-MOR catalyst.

**3.3.5  $\text{H}_2$ -TPR.** Fig. 7 shows the  $\text{H}_2$ -TPR results of Cu-SAPO-34 catalyst, and a broad band in the range of 275–800 °C is deconvoluted into three peaks at 345 °C, 440 °C and 585 °C, respectively. According to related literature reports,<sup>5,26</sup> the reduction of  $\text{Cu}^{2+}$  ions at the ion exchange site in the zeolites is divided into two steps: first,  $\text{Cu}^{2+}$  ions are reduced to  $\text{Cu}^+$  ions at



Table 2 Results of NH<sub>3</sub>-TPD and H<sub>2</sub>-TPR for fresh and aged samples

Samples	Desorbed NH <sub>3</sub> <sup>a</sup> (mmol g <sup>-1</sup> catalyst)			Total H <sub>2</sub> <sup>b</sup> consumption (mmol g <sup>-1</sup> catalyst)
	Peak $\alpha$	Peak $\beta$	Peak $\gamma$	
Cu-SAPO-34	0.28	0.12	0.19	1.86
Fe-MOR	0.09	0.25	—	0.69
Cu-SAPO-34@Fe-MOR	0.08	0.24	0.07	2.03
Cu-SAPO-34-750	0.23	0.15	0.16	1.05
Fe-MOR-750	0.23	0.18	—	—
Cu-SAPO-34@Fe-MOR-750	0.45	0.09	0.06	1.51

<sup>a</sup> The  $\alpha$ ,  $\beta$  and  $\gamma$  peaks respectively correspond to the weak, medium and strong acid sites, and are estimated from NH<sub>3</sub>-TPD data of the deconvoluted peaks. <sup>b</sup> The total H<sub>2</sub> consumption calculated from H<sub>2</sub>-TPR data.

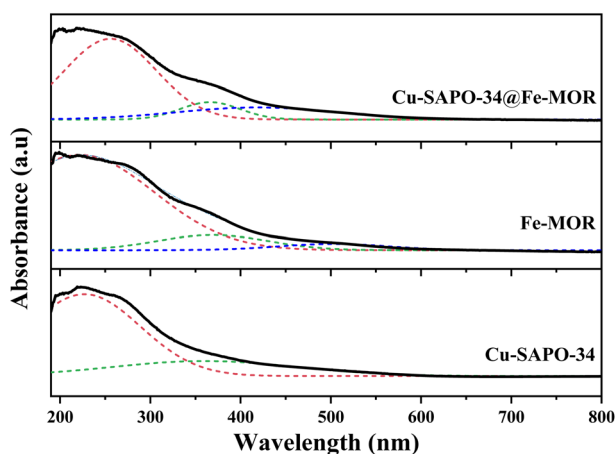
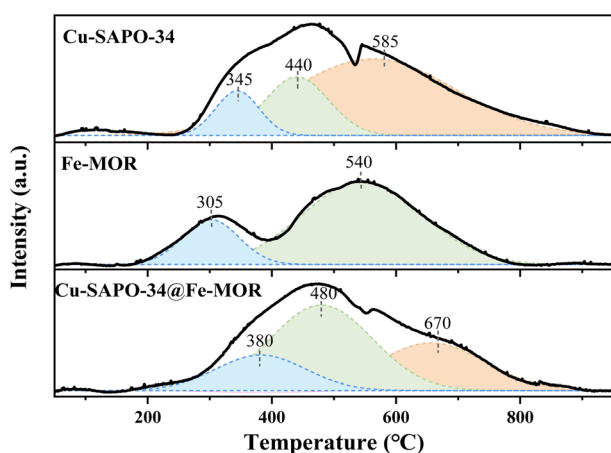


Fig. 6 UV-vis DRS spectra of Cu-SAPO-34, Fe-MOR and Cu-SAPO-34@Fe-MOR.

Fig. 7 H<sub>2</sub>-TPR profiles of Cu-SAPO-34, Fe-MOR and Cu-SAPO-34@Fe-MOR.

a lower temperature (the peak at 100–300 °C), and then Cu<sup>+</sup> ions are reduced to Cu<sup>0</sup> at a high temperature (the peak at 550–750 °C). The peak at 300–550 °C represents the reduction of copper oxide crystallites (in the zeolite channel) to Cu<sup>0</sup> in one step. By comparing the three reduction peaks of Cu-SAPO-34 it can be

found there are a large number of isolated Cu<sup>2+</sup> and Cu<sup>+</sup> ions at the ion exchange site and copper oxide crystallites in the zeolite channel. The H<sub>2</sub> reduction of Fe-MOR shows two reduction peaks in the temperature regions of 200–400 °C and 400–650 °C, which are attributed to the reduction of isolated Fe<sup>3+</sup> ions at the ion exchange site and the reduction of iron oxide oligomerization in the zeolite channel, respectively.<sup>29</sup> For Cu-SAPO-34@Fe-MOR catalyst, the H<sub>2</sub> reduction pattern is roughly similar to that of Cu-SAPO-34, which basically exhibits the reduction peak of isolated Cu<sup>2+</sup> and Cu<sup>+</sup> ions at the ion exchange site and copper oxide crystallites in the zeolite channel. Still, the reduction peak of Cu<sup>+</sup> ions (670 °C) and copper oxide (480 °C) move to higher temperature to some extent (35 °C and 85 °C, respectively) compared with that of Cu-SAPO-34, which may be caused by the coating of Fe-MOR on the surface and the synergistic interaction between the Cu<sup>2+</sup>/Fe<sup>3+</sup> ions on core-shell layer.

### 3.4 The effect of Fe-MOR coating on the core-shell catalyst

**3.4.1 Effect of Fe-MOR coating on the activity of the core-shell catalyst.** The results of NH<sub>3</sub>-SCR test (Fig. 2a) have shown that Cu-SAPO-34@Fe-MOR exhibits not only a wider reaction temperature window, but also a very good NO<sub>x</sub> reduction activity in high temperature region.

The NH<sub>3</sub>-TPD results (Fig. 5) have shown that the number of Lewis acid sites ( $\beta$  peaks) is significantly increased on Cu-SAPO-34@Fe-MOR, and this may contribute to its good catalytic activity as it is reported by previous research that Lewis acid sites with medium strength are more involved in the NH<sub>3</sub>-SCR reaction and have a good influence on the catalytic properties.<sup>11</sup> The results of UV-vis DRS (Fig. 6) have shown that the core-shell Cu-SAPO-34@Fe-MOR catalyst has many isolated Cu<sup>2+</sup> ions and Fe<sup>3+</sup> ions, which are the active species of NH<sub>3</sub>-SCR at low temperature and high temperature, respectively. This may also contribute to the broader temperature window of Cu-SAPO-34@Fe-MOR. H<sub>2</sub>-TPR results (Fig. 7) have shown that the H<sub>2</sub> reduction pattern of Cu-SAPO-34@Fe-MOR catalyst is similar to Cu-SAPO-34, exhibiting typical reduction of isolated Cu<sup>2+</sup> and Cu<sup>+</sup> ions and copper oxide crystallites in the zeolite channel. Especially, the reduction peak of Cu<sup>+</sup> ions (670 °C) and copper oxide (480 °C) over Cu-SAPO-34@Fe-MOR move to higher temperature, suggesting the synergistic interaction effect of the copper species and iron species on the catalyst after Fe-MOR



coating on the surface. This could be an important reason for the increased high-temperature activity and wider reaction temperature window of Cu-SAPO-34@Fe-MOR.

To further explore the influence of Fe-MOR coating on  $\text{Cu}^{2+}$  ions species and the synergistic interaction effect between the copper species and iron species on the catalytic processes, we conducted the *in situ* UV-vis transient dynamic studies on the oxidation and reduction half cycle over Cu-SAPO-34 and Cu-SAPO-34@Fe-MOR. As shown in Fig. 8(a and c), Cu-SAPO-34 and Cu-SAPO-34@Fe-MOR both exhibit classic oxidation half cycle over Cu-zeolites as previous reports.<sup>30,31</sup> After switching the atmosphere from  $\text{NO} + \text{NH}_3$  to  $\text{O}_2$ , the broad band above  $\sim 20\,000\text{ cm}^{-1}$  assigned to the d-d transition of  $\text{Cu}^{2+}$  ions arises, indicating the oxidation of  $\text{Cu}(\text{I})$  to  $\text{Cu}(\text{II})$  species over the catalysts.<sup>31</sup> Comparing the intensity changes of the d-d splitting of  $\text{Cu}(\text{II})$  between Fig. 8a and c, it is found that Cu-SAPO-34@Fe-MOR has more drastic changes of  $\text{Cu}(\text{II})$  d-d splitting strength compared with that of Cu-SAPO-34. These results reveal that the redox cycling ability of  $\text{Cu}^{2+}$  ions in Cu-SAPO-34@Fe-MOR is greatly enhanced after covering of Fe-MOR shells. Similar result is found in the reduction half cycle, as shown in Fig. 8b and d. After the atmosphere switched from  $\text{O}_2 + \text{NO}$  to  $\text{NH}_3$ , the intensity of d-d vibration of  $\text{Cu}(\text{II})$  species drops rapidly over the

two catalysts, with Cu-SAPO-34@Fe-MOR much more remarkably, accomplishing the reduction half cycle from  $\text{Cu}(\text{II})$  to  $\text{Cu}(\text{I})$  species. The *in situ* UV-vis transient studies have demonstrated that  $\text{Cu}(\text{II})$  ions species on Cu-SAPO-34@Fe-MOR has stronger redox ability, which may be another evidence or implication for the synergistic effect between the core-shell layers, and this finding is in line with the  $\text{H}_2$ -TPR results (Fig. 7). The higher redox ability of Cu-SAPO-34@Fe-MOR greatly promotes the catalytic oxidation and reduction half-reaction processes, which would make a significant contribution to its enhanced activity in  $\text{NH}_3$ -SCR.

Finally, as the adsorption capacity of the reactants will significantly affect the reaction performance of the catalysts, we carried out a  $\text{NO}$ -TPD experiment to measure the  $\text{NO}_x$  adsorption-desorption behavior over Cu and Fe zeolites. Fig. 9 shows the  $\text{NO}$  desorption peaks of Cu-SAPO-34 and Cu-SAPO-34@Fe-MOR. For all samples, the peaks below  $100\text{ }^\circ\text{C}$  are belonged to physical  $\text{NO}_x$  adsorption. The peak between  $100$  and  $200\text{ }^\circ\text{C}$  may be due to chemical desorption of  $\text{NO}_x$  or monodentate nitrate species. Peaks above  $200\text{ }^\circ\text{C}$  are attributed to desorption of bidentate nitrates or bridging nitrates.<sup>32,33</sup> Analyzing the results of  $\text{NO}$ -TPD on the core-shell Cu-SAPO-34@Fe-MOR, we can find that the physically adsorbed  $\text{NO}$  significantly increased, the

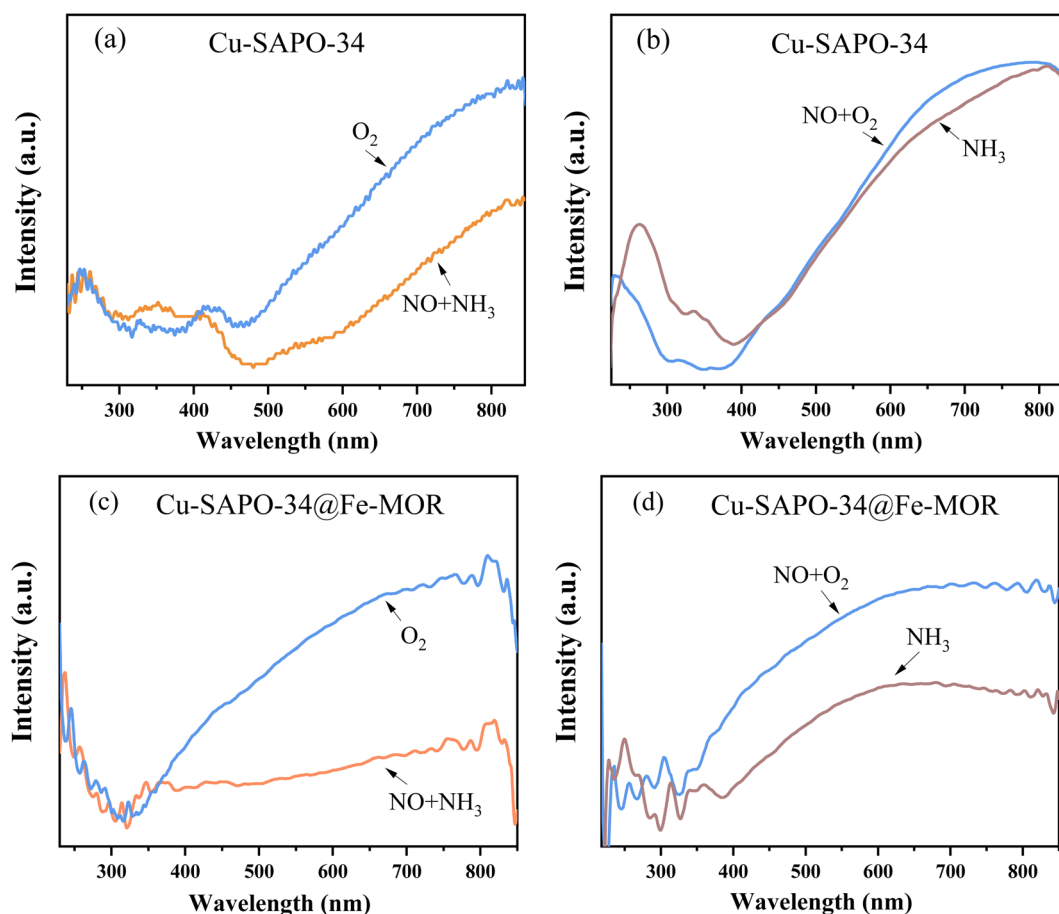


Fig. 8 *In situ* UV-vis transient dynamic studies over Cu-SAPO-34: oxidation half cycle (a) and reduction half cycle (b); *in situ* UV-vis transient dynamic studies over Cu-SAPO-34@Fe-MOR: oxidation half cycle (c) and reduction half cycle (d).



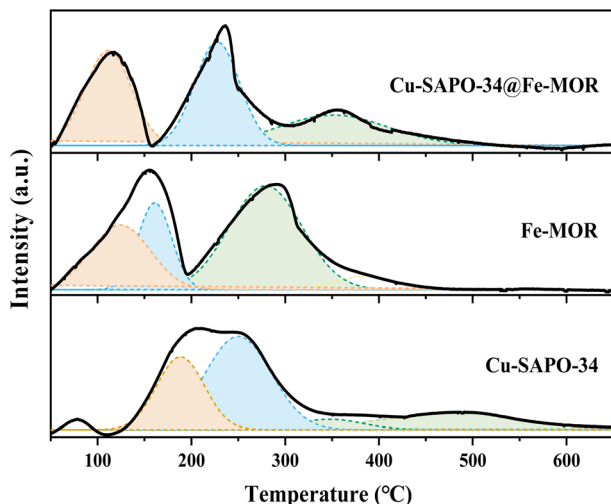


Fig. 9 NO-TPD results of Cu-SAPO-34, Fe-MOR and Cu-SAPO-34@Fe-MOR.

chemical desorption of  $\text{NO}_x$  or monodentate nitrate species moved towards lower temperatures, and the desorption of bidentate nitrates or bridging nitrates almost disappeared (above 400 °C), compared with Cu-SAPO-34. These results indicate that  $\text{NO}_x$  is more likely to form weakly adsorbed species over the core-shell composite and may be more approachable and participate in  $\text{NH}_3$ -SCR reaction.

Based on the above analysis, the reason why the introduction of Fe-MOR shell significantly widens the reaction temperature window of the composite and increases its activity at high temperature may involve the following aspects: first, large number of isolated  $\text{Cu}^{2+}$  ions and Fe ions on the ions exchange sites act as the active sites for  $\text{NO}_x$  reduction at low and high temperature region. Second, the synergistic interaction effect between the core and shell layer promotes the redox cycle of the catalyst and increases the oxidation–reduction ability of copper ions and further improves its high-temperature activity in core-shell Cu-SAPO-34@Fe-MOR. Moreover, number of Lewis acid sites on the core-shell catalyst is significantly increased, which may be another reason for its improved  $\text{NH}_3$ -SCR activity performance. Last,  $\text{NO}_x$  is more likely to form weakly adsorbed species on Cu-SAPO-34@Fe-MOR and maybe more approachable and participate in the  $\text{NH}_3$ -SCR reaction.

**3.4.2 Effect of Fe-MOR coating on hydrothermal stability of Cu-SAPO-34@Fe-MOR.** The results of the hydrothermal stability test (Fig. 2b) show that after hydrothermal treatment at 750 °C, the NO conversion rate of Cu-SAPO-34 has been significantly decreased, while Cu-SAPO-34@Fe-MOR maintains its activity much better in comparison. The catalysts after hydrothermal treatment at 750 °C were characterized to further explore the influence of core-shell structure on hydrothermal stability of the catalyst.

$\text{N}_2$  adsorption–desorption isotherms of the catalysts after hydrothermal ageing is shown in Fig. S3† and their BET data are present in Table 1. After Fe-MOR coating, the core-shell Cu-SAPO-34@Fe-MOR catalyst maintains much better BET

specific surface area and pore volume, indicating that Fe-MOR and Cu-SAPO-34@Fe-MOR have a lighter structural collapse after hydrothermal ageing. Fig. 10 and Table 2 have shown  $\text{NH}_3$ -TPD analysis of samples after hydrothermal aging. The intensity of the desorption peaks of all samples is weakened after hydrothermal ageing, which may be due to the partial collapse of the internal structure of the catalyst caused by the hydrothermal treatment. The core-shell Cu-SAPO-34@Fe-MOR has shown much lower acid loss (52%) after hydrothermal ageing compared with Cu-SAPO-34 (12%), indicating the core-shell catalyst may maintain its internal structure better, and this result is in line with its higher activity maintenance degree.

The UV-vis-DRS spectra of the catalysts after hydrothermal ageing treatment are shown in Fig. 11a. The absorption intensity of Cu-SAPO-34@Fe-MOR-750 at 200–350 nm is slightly stronger than that of Cu-SAPO-34, indicating more isolated  $\text{Cu}^{2+}$  ions existing in Cu-SAPO-34@Fe-MOR-750 after hydrothermal ageing. This inhibiting loss of isolated copper ions during hydrothermal treatment in the core-shell catalyst may be ascribed to the protective effect of the Fe-MOR shell and contribute to its better activity retention. The  $\text{H}_2$ -TPR analysis on the hydrothermally aged catalyst is shown in Fig. 11b. Cu-SAPO-34@Fe-MOR-750 has a more obvious reduction peak at 250–400 °C compared with aged Cu-SAPO-34, declaring more isolated  $\text{Cu}^{2+}$  and  $\text{Fe}^{3+}$  ions remained in the core-shell catalyst after ageing. These results are consistent with the UV-vis-DRS spectra, and prove that more isolated copper and iron ions kept in core-shell catalyst after ageing, which may contribute to the better catalytic activity of Cu-SAPO-34@Fe-MOR-750 compared with Cu-SAPO-34-750. NO-TPD results of Cu-SAPO-34-750 and Cu-SAPO-34@Fe-MOR-750 are shown in Fig. 12. Compared with the fresh catalyst, the chemical desorption of  $\text{NO}_x$  or monodentate nitrate species (180–350 °C) of the samples after hydrothermal ageing all move to higher temperature, which indicates that the  $\text{NO}_x$  adsorbed species on the aged

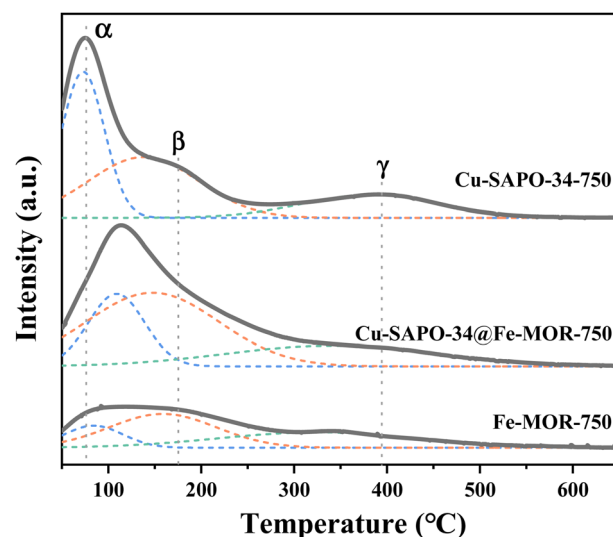


Fig. 10  $\text{NH}_3$ -TPD spectra of Cu-SAPO-34-750 and Cu-SAPO-34@Fe-MOR-750.



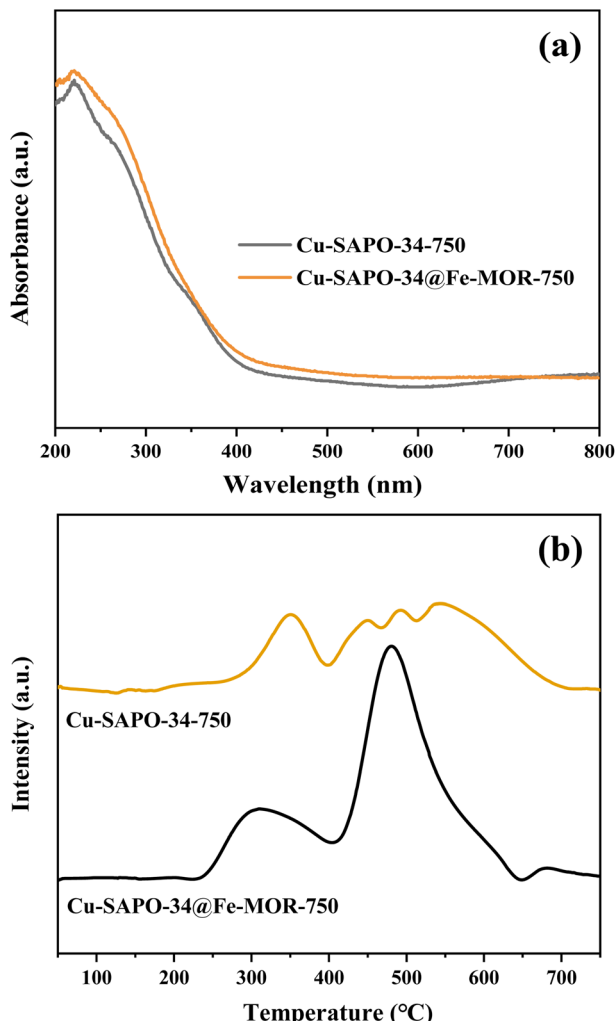


Fig. 11 UV-vis DRS (a) and H<sub>2</sub>-TPR spectra (b) of Cu-SAPO-34-750 and Cu-SAPO-34@Fe-MOR-750.

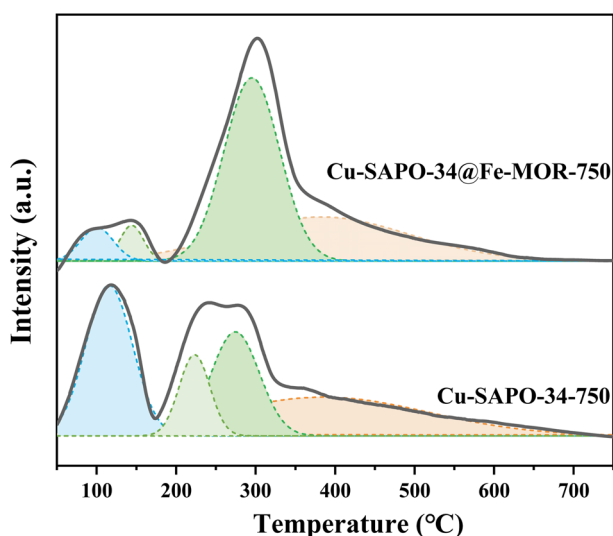


Fig. 12 NO-TPD spectra of Cu-SAPO-34-750 and Cu-SAPO-34@Fe-MOR-750.

samples are less accessible and more likely to cause the accumulation of refractory nitrates. This might constitute one reason for their decreased activities. Cu-SAPO-34@Fe-MOR-750 has much higher chemical desorption of NO<sub>x</sub> or monodentate nitrate species than Cu-SAPO-34-750, which is also in line with its higher activity for NH<sub>3</sub>-SCR.

According to all the above characteristic analyses, it can be concluded that superior hydrothermal aging stability of Cu-SAPO-34@Fe-MOR compared with Cu-SAPO-34 may be due to: first, by the protection of shell layer, Cu-SAPO-34@Fe-MOR have a lighter structural collapse after hydrothermal ageing and maintains much better BET specific surface area and pore volume. Second, the protective effect of Fe-MOR shell inhibits the loss of acidic sites and isolated copper ions during hydrothermal treatment, and there are still more active components (Cu<sup>2+</sup> and Fe<sup>3+</sup>) and acidic sites in the core-shell catalyst after ageing. Last, Cu-SAPO-34@Fe-MOR-750 keeps much higher chemical desorption of NO<sub>x</sub> or monodentate nitrate species, further contributing to its higher activity for NH<sub>3</sub>-SCR.

### 3.5 Reaction mechanism studies of core-shell Cu-SAPO-34@Fe-MOR

The reaction mechanism on the core-shell catalysts was investigated in detail by *in situ* DRIFTS transient analysis, to reveal the nature of the enhanced catalytic performance of core-shell catalysts and the role of core-shell structure.

**3.5.1 Adsorption of NH<sub>3</sub>.** As we all know, the NH<sub>3</sub> species is important in the NH<sub>3</sub>-SCR reaction. To further explore the NH<sub>3</sub> species adsorbed on the catalyst, the *in situ* DRIFTS for NH<sub>3</sub> adsorption over Cu-zeolites are shown in Fig. 13a. Cu-SAPO-34 has prominent absorption peaks at 3630–3300 cm<sup>−1</sup> and 1450–1200 cm<sup>−1</sup>. The adsorption bands at 3628 and 3598 cm<sup>−1</sup> represent the vibration modes of Si–OH and Si–O–Al at Brønsted acid sites, respectively.<sup>34</sup> The bands at 3398 and 3300 cm<sup>−1</sup> correspond to the tensile vibration mode of N–H coordinated with NH<sub>3</sub> at the Brønsted acid site.<sup>35</sup> The band changed at 1450 and 1350 cm<sup>−1</sup> are attributed to the symmetric bending vibration of the NH<sub>4</sub><sup>+</sup> species at the Brønsted acid site.<sup>36</sup> The adsorptions at 1300 and 1200 cm<sup>−1</sup> are caused by the symmetrical deformation of NH<sub>3</sub> coordinated with two different types of cations on Lewis acid sites.<sup>35</sup> Fig. 13b is the *in situ* DRIFTS spectra of NH<sub>3</sub> adsorption over Cu-SAPO-34@Fe-MOR. Adsorption bands at 3630–3300 cm<sup>−1</sup>, 1300 cm<sup>−1</sup> and 1200 cm<sup>−1</sup> are also observed similar to that of Cu-SAPO-34 (Fig. 13a). New adsorption bands shown at 1495 cm<sup>−1</sup> correspond to the symmetric bending vibration of the NH<sub>4</sub><sup>+</sup> species at the Brønsted acid site.<sup>37</sup> The band at 1375 cm<sup>−1</sup> may be related to the amide (–NH<sub>2</sub>) species.<sup>35</sup> The new absorption at 998 cm<sup>−1</sup> is ascribed to NH<sub>3</sub>–Cu<sup>2+</sup> species formed by the adsorption of NH<sub>3</sub> on Cu<sup>2+</sup> cations.<sup>35</sup> For comparison, it is found not only more abundant NH<sub>3</sub> adsorption species are found, but also more rapid adsorption saturation is reached on the core-shell Cu-SAPO-34@Fe-MOR catalyst. All the NH<sub>3</sub> species adsorbed on the surface of Cu-SAPO-34@Fe-MOR have reached saturation below 3 minutes,



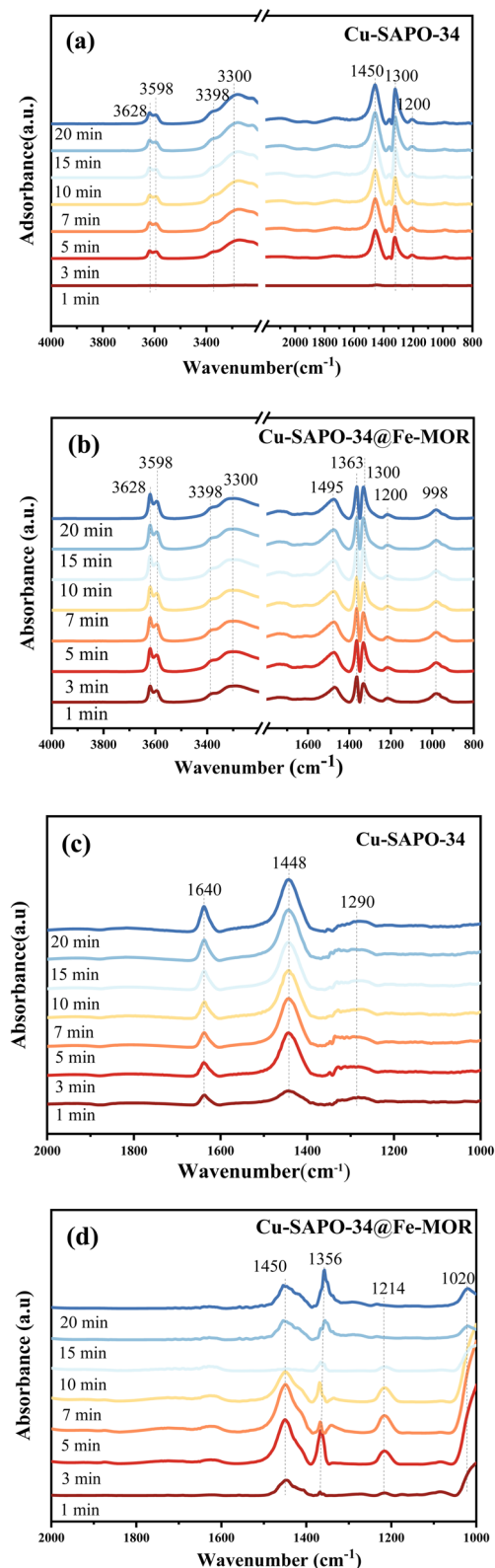


Fig. 13 *In situ* DRIFTS of  $\text{NH}_3$  adsorption over Cu-SAPO-34 (a) and Cu-SAPO-34@Fe-MOR (b); *in situ* DRIFTS of  $\text{NO} + \text{O}_2$  adsorption over Cu-SAPO-34 (c) and Cu-SAPO-34@Fe-MOR (d).

while for Cu-SAPO-34 several hard to adsorbed  $\text{NH}_3$  species have taken for above 10 minutes. Those more abundant and more easily adsorbed  $\text{NH}_3$  species on the core-shell Cu-SAPO-

34@Fe-MOR catalyst may play a beneficial role in its higher activity compared with that of Cu-SAPO-34.<sup>37,38</sup>

**3.5.2 Adsorption of  $\text{NO} + \text{O}_2$ .** The *in situ* DRIFTS for  $\text{NO} + \text{O}_2$  co-adsorption on Cu-SAPO-34 and Cu-SAPO-34@Fe-MOR are shown in Fig. 13c and d to reveal the adsorption behavior of various  $\text{NO}_x$  species on the surface of the catalysts. The *in situ* DRIFTS spectrum of Cu-SAPO-34 has shown three bands of adsorbed  $\text{NO}_x$  species at 1640, 1448, and 1295  $\text{cm}^{-1}$ , respectively. The bands at 1640  $\text{cm}^{-1}$  and 1295  $\text{cm}^{-1}$  are attributed to bridging nitrate species.<sup>39</sup> The band of 1448  $\text{cm}^{-1}$  is caused by the monodentate nitrate species.<sup>40</sup> As shown in Fig. 13d, Cu-SAPO-34@Fe-MOR has shown four new bands of adsorbed  $\text{NO}_x$  species at 1450, 1352, 1208 and 1023  $\text{cm}^{-1}$ , which may be related to monodentate nitrate species, chelated nitrite, monodentate nitrate species, and bidentate nitrate species, respectively.<sup>39–42</sup> This result indicates that more intermediate nitrate species are formed and adsorbed on the surface of core-shell Cu-SAPO-34@Fe-MOR catalyst compared with Cu-SAPO-34. And this finding is consistent with the result of  $\text{NO}$ -TPD, indicating that on Cu-SAPO-34@Fe-MOR  $\text{NO}_x$  forms weaker adsorbed monodentate nitrate and may be more approachable and participate in  $\text{NO}_x$  reduction. This also supports the better activities performance of Cu-SAPO-34@Fe-MOR.

**3.5.3 *In situ* DRIFTS studies for Cu-SAPO-34.** Fig. 14a shows the *in situ* DRIFTS spectra of  $\text{NO} + \text{O}_2$  reacting with the pre-adsorbed  $\text{NH}_3$  on the surface of Cu-SAPO-34. After saturated with  $\text{NH}_3$  species, the main adsorbed species are  $\text{NH}_3$  species adsorbed on Si–O–Al (3598  $\text{cm}^{-1}$ ) and Si–OH (3628  $\text{cm}^{-1}$ ),<sup>34</sup> the tensile vibration mode of N–H coordinated with  $\text{NH}_3$  at the Brønsted acid site (3398 and 3300  $\text{cm}^{-1}$ ) and  $\text{NH}_4^+$  species (1450  $\text{cm}^{-1}$ ) on Brønsted acid site,<sup>35,36</sup>  $\text{NH}_3$  species (1300 and 1200  $\text{cm}^{-1}$ ) on Lewis acid site.<sup>35</sup> When  $\text{NO} + \text{O}_2$  is introduced, Lewis acid site (1300  $\text{cm}^{-1}$ ) gradually depletes with time. In contrast, the peak intensity of the Brønsted acid site (1450  $\text{cm}^{-1}$ ) remains basically unchanged, indicating that Lewis acid site is the main active acidic sites involved in the SCR reaction on Cu-SAPO-34 catalyst. Fig. 14c shows the *in situ* DRIFTS spectra of  $\text{NH}_3$  reacting with the pre-adsorbed  $\text{NO} + \text{O}_2$  on the surface of Cu-SAPO-34. First, after the saturation of pre-adsorbed  $\text{NO} + \text{O}_2$ , the spectra show band changes at 1637  $\text{cm}^{-1}$  and 1430  $\text{cm}^{-1}$ , representing bridged nitrate and monodentate nitrate, respectively.<sup>39,40</sup> With the introduction of  $\text{NH}_3$ , the bridge nitrate species (1640  $\text{cm}^{-1}$ ) and monodentate nitrate (1430  $\text{cm}^{-1}$ ) decrease gradually and disappear with the appearance of the bands attributed to various  $\text{NH}_3$  species, which gradually increase with the adsorption time. The process indicates that the adsorbed state  $\text{NO}_x$  reacts rapidly with  $\text{NH}_3$ , the adsorbed nitrate species has high reactivity over Cu-SAPO-34, following Langmuir–Hinshelwood (“L–H”) mechanism in the  $\text{NH}_3$ -SCR reaction over Cu-SAPO-34 catalyst.

**3.5.4 *In situ* DRIFTS transient studies for Cu-SAPO-34 @Fe-MOR.** Fig. 14b is the *in situ* DRIFTS spectrum of  $\text{NO} + \text{O}_2$  reacting with pre-adsorbed  $\text{NH}_3$  over Cu-SAPO-34@Fe-MOR. When the adsorbed  $\text{NH}_3$  is saturated,  $\text{NH}_3$  on Si–O–Al and Si–OH (3598 and 3628  $\text{cm}^{-1}$ ),  $\text{NH}_4^+$  species (1730 and 1495  $\text{cm}^{-1}$ ) on Brønsted acid sites and the tensile vibration mode of N–H coordinated with  $\text{NH}_3$  at the Brønsted acid site (3398,



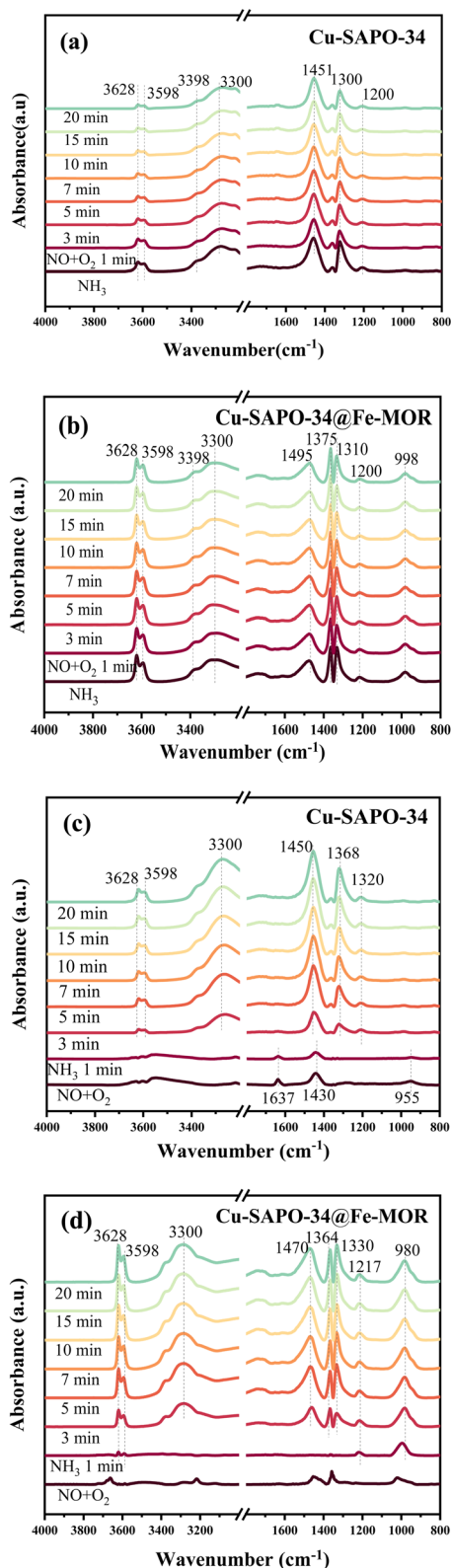


Fig. 14 *In situ* DRIFTS transient studies for  $\text{NO}_x$  reacting with pre-adsorbed  $\text{NH}_3$  over Cu-SAPO-34 (a) and Cu-SAPO-34@Fe-MOR (b); *in situ* DRIFTS transient studies for  $\text{NH}_3$  reacting with pre-adsorbed  $\text{NO}_x$  over Cu-SAPO-34 (c) and Cu-SAPO-34@Fe-MOR (d).

$3300\text{ cm}^{-1}$ ),  $\text{NH}_3$  species ( $1310$  and  $1200\text{ cm}^{-1}$ ) on Lewis acid sites, and the amide ( $-\text{NH}_2$ ) species ( $1375\text{ cm}^{-1}$ ) are the main adsorbed species. No obvious nitrate species appear after the introduction of  $\text{NO} + \text{O}_2$ . The changing trend of  $\text{NH}_3$  species adsorbed on the surface is basically the same as that of Cu-SAPO-34 (Fig. 14a). The  $\text{NH}_4^+$  species on the Lewis acid site is the main reaction intermediate. Fig. 14d shows the *in situ* DRIFTS spectra of the reaction between pre-adsorbed  $\text{NO} + \text{O}_2$  with  $\text{NH}_3$  over Cu-SAPO-34@Fe-MOR. After co-adsorption of  $\text{NO} + \text{O}_2$ , monodentate nitrate ( $1450\text{ cm}^{-1}$ ) and chelated nitrate ( $1356\text{ cm}^{-1}$ ) appear.<sup>39</sup> The band attributed to nitrate disappears rapidly when  $\text{NH}_3$  is introduced for 1 minute, and  $\text{NH}_3\text{-Cu}^{2+}$  species ( $990\text{ cm}^{-1}$ ) appears.<sup>35</sup> Absorption peaks of various  $\text{NH}_3$  species appear at 5 minutes, and the intensity increases with time. This reaction process is similar to Cu-SAPO-34, indicating that Cu-SAPO-34@Fe-MOR also follows the “L-H” mechanism for  $\text{NH}_3$ -SCR. In addition, over the Cu-SAPO-34@Fe-MOR additional amide ( $-\text{NH}_2$ ) species ( $1375\text{ cm}^{-1}$ ) show up and react with the introduced  $\text{NO} + \text{O}_2$ , which suggests this reaction may also follow the Eley-Rideal (“E-R”) reaction pathway.<sup>35</sup> Therefore, it is possible that both “L-H” and “E-R” mechanisms play a role in Cu-SAPO-34@Fe-MOR, which might also contribute to higher activity of Cu-SAPO-34@Fe-MOR compared with Cu-SAPO-34.

## 4. Conclusions

In this study, a core-shell catalyst of Cu-SAPO-34@Fe-MOR was successfully prepared through the silica-sol adhesion method, and its performance for  $\text{NH}_3$ -SCR was evaluated in detail. The coating of Fe-MOR has not only increased the high temperature activity and broadened the reaction temperature window of Cu-SAPO-34 to a large extent, but also increased the hydrothermal stability of Cu-SAPO-34 markedly. The analysis of *in situ* UV-vis transient studies and  $\text{H}_2$ -TPR have demonstrated that a strong synergistic interaction effect exists between  $\text{Cu}^{2+}$  ions and Fe ions and promotes the redox cycle and oxidation-reduction ability of copper ions. On the other hand, after hydrothermal aging the core-shell Cu-SAPO-34@Fe-MOR catalyst exhibits lighter structural collapse, less acidic sites lost, more active components ( $\text{Cu}^{2+}$  and  $\text{Fe}^{3+}$ ) maintained, and more monodentate nitrate species formed, which may contribute its better hydrothermal ageing stability. Last, the mechanisms study has found that both Langmuir-Hinshelwood (“L-H”) and Eley-Rideal (“E-R”) mechanisms play an important role on Cu-SAPO-34@Fe-MOR, and constitute another reason for its increased activity after Fe-MOR coating (mainly “L-H” mechanisms for Cu-SAPO-34).

## Conflicts of interest

There are no conflicts to declare.

## Acknowledgements

This work is financially supported by the General Project of Natural Science Foundation of Jilin Province (20220101094JC).





and General Program of Chongqing Natural Science Foundation (CSTB2022NSCQ-MSX0412).

## References

- 1 Y. J. Pu, X. Y. Xie, W. J. Jiang, L. Yang, X. Jiang and L. Yao, Low-temperature selective catalytic reduction of NO<sub>x</sub> with NH<sub>3</sub> over zeolite catalysts: A review, *Chin. Chem. Lett.*, 2020, **31**, 2549–2555, DOI: [10.1016/j.ccl.2020.04.012](#).
- 2 X. F. Wang, Y. Xu, Z. Zhao, J. B. Liao, C. Chen and Q. B. Li, Recent progress of metal-exchanged zeolites for selective catalytic reduction of NO<sub>x</sub> with NH<sub>3</sub> in diesel exhaust, *Fuel*, 2021, **305**, 121482, DOI: [10.1016/j.fuel.2021.121482](#).
- 3 S. Mahalingam, A. Murugesan, T. Thiruppathiraja, S. Lakshmipathi, T. R. Makhanya and R. M. Gengan, Green synthesis of benzimidazole derivatives by using zinc boron nitride catalyst and their application from DFT (B3LYP) study, *Heliyon*, 2022, **8**(11), e11480, DOI: [10.1016/j.heliyon.2022.e11480](#).
- 4 H. Jouini, I. Mejri, J. Martinez-Ortigosa, J. L. Cerrillo, M. Mhamdia, A. E. Palomares, G. Delahay and T. Blasco, Selective catalytic reduction of nitric oxide with ammonia over Fe-Cu modified highly silicated zeolites, *Solid State Sci.*, 2018, **84**, 75–85, DOI: [10.1016/j.solidstatesciences.2018.08.008](#).
- 5 H. W. Zhao, H. S. Li, X. H. Li, M. K. Liu and Y. D. Li, The promotion effect of Fe to Cu-SAPO-34 for selective catalytic reduction of NO<sub>x</sub> with NH<sub>3</sub>, *Catal. Today*, 2017, **297**, 84–91, DOI: [10.1016/j.cattod.2017.05.060](#).
- 6 R. Ghosh Chaudhuri and S. Paria, Core/shell nanoparticles: classes, properties, synthesis mechanisms, characterization, and applications, *Chem. Rev.*, 2012, **112**, 2373–2433, DOI: [10.1021/cr100449n](#).
- 7 K. M. Hassan, L. Y. Mehmet, A. Necip, O. Yasin, K. Fatemeh, P. S. Kumar, R. Jalal and B. Mehdi, A novel detection method for organophosphorus insecticide fenamiphos: Molecularly imprinted electrochemical sensor based on core-shell Co<sub>3</sub>O<sub>4</sub>@MOF-74 nanocomposite, *J. Colloid Interface Sci.*, 2021, **592**, 174–185, DOI: [10.1016/j.jcis.2021.02.066](#).
- 8 L. Chen, X. X. Wang, Q. L. Cong, H. Y. Ma, S. J. Li and W. Li, Design of a hierarchical Fe-ZSM-5@CeO<sub>2</sub> catalyst and the enhanced performances for the selective catalytic reduction of NO with NH<sub>3</sub>, *Chem. Eng. J.*, 2019, **369**, 957–967, DOI: [10.1016/j.cej.2019.03.055](#).
- 9 N. Rajkoomar, A. Murugesan, S. Prabu and R. M. Gengan, Synthesis of methyl piperazinyl-quinolinyl  $\alpha$ -aminophosphonates derivatives under microwave irradiation with Pd-SrTiO<sub>3</sub> catalyst and their antibacterial and antioxidant activities, *Phosphorus Sulfur Silicon Relat. Elem.*, 2020, **195**, 1031–1038, DOI: [10.1080/10426507.2020.1799366](#).
- 10 T. Thiruppathiraja, A. L. Arokiyanathan and S. Lakshmipathi, Pyrrolic, pyridinic, and graphitic sumanene as metal-free catalyst for oxygen reduction reaction—A density functional theory study, *Fuel Cells*, 2021, **21**, 490–501, DOI: [10.1002/fuce.202100004](#).
- 11 T. Y. Du, H. X. Qu, Q. Liu, Q. Zhong and W. H. Ma, Synthesis, activity and hydrophobicity of Fe-ZSM-5@silicalite-1 for NH<sub>3</sub>-SCR, *Chem. Eng. J.*, 2015, **262**, 1199–1207, DOI: [10.1016/j.cej.2014.09.119](#).
- 12 Z. Q. Chen, L. Liu, H. X. Qu, B. J. Zhou, H. F. Xie and Q. Zhong, Migration of cations and shell functionalization for Cu-Ce-La/SSZ-13@ZSM-5: The contribution to activity and hydrothermal stability in the selective catalytic reduction reaction, *J. Catal.*, 2020, **392**, 217–230, DOI: [10.1016/j.jcat.2020.10.005](#).
- 13 M. Y. Chen, Y. Z. Wei, J. F. Han, W. F. Yan and J. J. Yu, Enhancing catalytic performance of Cu-SSZ-13 for the NH<sub>3</sub>-SCR reaction *via in situ* introduction of Fe<sup>3+</sup> with diatomite, *Mater. Chem. Front.*, 2021, **5**, 7787–7795, DOI: [10.1039/D1QM01101D](#).
- 14 Z. Y. Di, H. Wang, R. D. Zhang, H. G. Chen, Y. Wei and J. B. Jia, ZSM-5 core-shell structured catalyst for enhancing low-temperature NH<sub>3</sub>-SCR efficiency and poisoning resistance, *Appl. Catal., A*, 2022, **630**, 118438, DOI: [10.1016/j.apcata.2021.118438](#).
- 15 G. H. Yang, C. Xing, W. Hirohama, Y. Z. Jin, C. Y. Zeng, Y. Suehiro, T. J. Wang, Y. Yoneyama and N. Tsubaki, Tandem catalytic synthesis of light isoparaffin from syngas *via* Fischer-Tropsch synthesis by newly developed core-shell-like zeolite capsule catalysts, *Catal. Today*, 2013, **215**, 29–35, DOI: [10.1016/j.cattod.2013.01.010](#).
- 16 H. R. Mahmoud, S. A. El-Molla and M. A. Naghmash, Novel mesoporous MnO<sub>2</sub>/SnO<sub>2</sub> nanomaterials synthesized by ultrasonic-assisted co-precipitation method and their application in the catalytic decomposition of hydrogen peroxide, *Ultrasonics*, 2019, **95**, 95–103, DOI: [10.1016/j.ultras.2019.03.011](#).
- 17 H. I. Hamoud, V. Valtchev and M. Daturi, Selective catalytic reduction of NO<sub>x</sub> over Cu- and Fe-exchanged zeolites and their mechanical mixture, *Appl. Catal., B*, 2019, **250**, 419–428, DOI: [10.1016/j.apcatb.2019.02.022](#).
- 18 Y. H. Ma, H. W. Zhao, C. J. Zhang, Y. N. Zhao, H. Chen and Y. D. Li, Enhanced hydrothermal stability of Cu-SSZ-13 by compositing with Cu-SAPO-34 in selective catalytic reduction of nitrogen oxides with ammonia, *Catal. Today*, 2020, **355**, 627–634, DOI: [10.1016/j.cattod.2019.03.057](#).
- 19 M. Iwasaki, K. Yamazaki and H. Shinjoh, NO<sub>x</sub> reduction performance of fresh and aged Fe-zeolites prepared by CVD: Effects of zeolite structure and Si/Al<sub>2</sub> ratio, *Appl. Catal., B*, 2011, **102**, 302–309, DOI: [10.1016/j.apcatb.2010.12.016](#).
- 20 B. Guan, H. Jiang, X. S. Peng, Y. F. Wei, Z. Q. Liu, T. Chen, H. Lin and Z. Huang, Promotional effect and mechanism of the modification of Ce on the enhanced NH<sub>3</sub>-SCR efficiency and the low temperature hydrothermal stability over Cu-SAPO-34 catalysts, *Appl. Catal., A*, 2021, **617**, 118110, DOI: [10.1016/j.apcata.2021.118110](#).
- 21 H. M. Wang, W. Li, S. Y. Xu, M. Liu, J. M. Hao, P. Ning and Q. L. Zhang, Insights into the impact of lanthanum on hydrothermal-induced migration and transformation of copper species in Cu-SAPO-34 catalyst for NH<sub>3</sub>-SCR, *Mol. Catal.*, 2021, **515**, 111914, DOI: [10.1016/j.mcat.2021.111914](#).



- 22 J. Woo, A. Wang, D. Bernin, H. Ahari, M. Shost, M. Zammit and L. Olsson, Impact of different synthesis methods on the low-temperature deactivation of Cu/SAPO-34 for NH<sub>3</sub>-SCR reaction, *Emiss. Control Sci. Technol.*, 2021, **7**, 198–209, DOI: [10.1007/s40825-020-00182-y](https://doi.org/10.1007/s40825-020-00182-y).
- 23 Z. Y. Sheng, Y. Chen, L. Yang, L. M. Yu and K. Zhuang, Cerium modified copper-based mordenite zeolite catalyst for high-temperature selective catalytic reduction NO with NH<sub>3</sub> of gas turbines, *React. Kinet., Mech. Catal.*, 2022, **135**, 723–739, DOI: [10.1007/s11144-022-02164-3](https://doi.org/10.1007/s11144-022-02164-3).
- 24 S. Zhang, S. J. Ming, L. Guo, C. Bian, Y. Meng, Q. Liu, Y. Dong, J. J. Bi, D. Li, Q. Wu, K. W. Qin, Z. Chen, L. Pang, W. Q. Cai and T. Li, Controlled synthesis of Cu-based SAPO-18/34 intergrowth zeolites for selective catalytic reduction of NO<sub>x</sub> by ammonia, *J. Hazard. Mater.*, 2021, **414**, 125543, DOI: [10.1016/j.jhazmat.2021.125543](https://doi.org/10.1016/j.jhazmat.2021.125543).
- 25 P. L. Wang, L. J. Yan, Y. D. Gu, S. Kuboon, H. R. Li, T. T. Yan, L. Y. Shi and D. S. Zhang, Poisoning-resistant NO<sub>x</sub> reduction in the presence of alkaline and heavy metals over H-SAPO-34-Supported Ce-promoted Cu-based catalysts, *Environ. Sci. Technol.*, 2020, **54**, 6396–6405, DOI: [10.1021/acs.est.0c00100](https://doi.org/10.1021/acs.est.0c00100).
- 26 R. Li, P. Q. Wang, S. B. Ma, F. L. Yuan, Z. B. Li and Y. J. Zhu, Excellent selective catalytic reduction of NO<sub>x</sub> by NH<sub>3</sub> over Cu/SAPO-34 with hierarchical pore structure, *Chem. Eng. J.*, 2020, **379**, 122376, DOI: [10.1016/j.cej.2019.122376](https://doi.org/10.1016/j.cej.2019.122376).
- 27 K. P. Xie, J. Woo, D. Bernin, A. Kumar, K. Kamasamudram and L. Olsson, Insights into hydrothermal aging of phosphorus-poisoned Cu-SSZ-13 for NH<sub>3</sub>-SCR, *Appl. Catal., B*, 2019, **241**, 205–216, DOI: [10.1016/j.apcatb.2018.08.082](https://doi.org/10.1016/j.apcatb.2018.08.082).
- 28 D. Pietrogiamici, M. C. Campa, L. R. Carbone and M. Occhiuzzi, N<sub>2</sub>O decomposition and reduction on Co-MOR, Fe-MOR and Ni-MOR catalysts: *in situ* UV-vis DRS and operando FTIR investigation. An insight on the reaction pathways, *Appl. Catal., B*, 2019, **240**, 19–29, DOI: [10.1016/j.apcatb.2018.08.046](https://doi.org/10.1016/j.apcatb.2018.08.046).
- 29 S. S. R. Putluru, L. Schill, A. D. Jensen and R. S. N. Fehrmann, Selective catalytic reduction of NO<sub>x</sub> with NH<sub>3</sub> on Cu-, Fe-, and Mn-zeolites prepared by impregnation: Comparison of activity and hydrothermal stability, *J. Chem.*, 2018, **2018**, 1–11, DOI: [10.1155/2018/8614747](https://doi.org/10.1155/2018/8614747).
- 30 C. Negri, M. Signorile, N. G. Porcaro, E. Borfecchia, G. Berlier, T. V. W. Janssens and S. Bordiga, Dynamic Cu<sup>II</sup>/Cu<sup>I</sup> speciation in Cu-CHA catalysts by *in situ* Diffuse Reflectance UV-vis-NIR spectroscopy, *Appl. Catal., A*, 2019, **578**, 1–9, DOI: [10.1016/j.apcata.2019.03.018](https://doi.org/10.1016/j.apcata.2019.03.018).
- 31 C. Liu, H. Kubota, T. Amada, K. Kon, T. Toyao, Z. Maeno, K. Ueda, J. Ohyama, A. Satsuma, T. Tanigawa, N. Tsumoji, T. Sano and K. I. Shimizu, *In situ* spectroscopic studies on the redox cycle of NH<sub>3</sub>-SCR over Cu-CHA zeolites, *ChemCatChem*, 2020, **12**, 3050–3059, DOI: [10.1002/cctc.202000024](https://doi.org/10.1002/cctc.202000024).
- 32 H. M. Wang, P. Ning, Y. Q. Zhang, Y. P. Ma, J. F. Wang, L. Y. Wang and Q. L. Zhang, Highly efficient WO<sub>3</sub>-FeO<sub>x</sub> catalysts synthesized using a novel solvent-free method for NH<sub>3</sub>-SCR, *J. Hazard. Mater.*, 2020, **388**, 121812, DOI: [10.1016/j.jhazmat.2019.121812](https://doi.org/10.1016/j.jhazmat.2019.121812).
- 33 Y. Z. Bai, J. H. Zhu, H. J. Luo, Z. F. Wang, Z. J. Gong, R. Zhao, W. F. Wu and K. Zhang, Study on NH<sub>3</sub>-SCR performance and mechanism of Fe/Mn modified rare earth concentrate, *Mol. Catal.*, 2021, **514**, 111665, DOI: [10.1016/j.mcat.2021.111665](https://doi.org/10.1016/j.mcat.2021.111665).
- 34 W. S. Chen, Z. Li, F. L. Hu, L. B. Qin, J. Han and G. M. Wu, *In situ* DRIFTS investigation on the selective catalytic reduction of NO with NH<sub>3</sub> over the sintered ore catalyst, *Appl. Surf. Sci.*, 2018, **439**, 75–81, DOI: [10.1016/j.apsusc.2018.01.057](https://doi.org/10.1016/j.apsusc.2018.01.057).
- 35 Q. L. Zhang, H. M. Wang, P. Ning, Z. X. Song, X. Liu and Y. K. Duan, *In situ* DRIFTS studies on CuO-Fe<sub>2</sub>O<sub>3</sub> catalysts for low temperature selective catalytic oxidation of ammonia to nitrogen, *Appl. Surf. Sci.*, 2017, **419**, 733–743, DOI: [10.1016/j.apsusc.2017.05.056](https://doi.org/10.1016/j.apsusc.2017.05.056).
- 36 G. Qi and R. T. Yang, Characterization and FTIR studies of MnO<sub>x</sub>-CeO<sub>2</sub> catalyst for low-temperature selective catalytic reduction of NO with NH<sub>3</sub>, *J. Phys. Chem. B*, 2004, **108**(40), 15738–15747, DOI: [10.1021/jp048431h](https://doi.org/10.1021/jp048431h).
- 37 Y. L. Shan, Y. Sun, J. P. Du, Y. Zhang, X. Y. Shi, Y. B. Yu, W. P. Shan and H. He, Hydrothermal aging alleviates the inhibition effects of NO<sub>2</sub> on Cu-SSZ-13 for NH<sub>3</sub>-SCR, *Appl. Catal., B*, 2020, **275**, 119105, DOI: [10.1016/j.apcatb.2020.119105](https://doi.org/10.1016/j.apcatb.2020.119105).
- 38 Y. Z. Xi, N. A. Ottinger, C. J. Keturakis and Z. G. Liu, Dynamics of low temperature N<sub>2</sub>O formation under SCR reaction conditions over a Cu-SSZ-13 catalyst, *Appl. Catal., B*, 2021, **294**, 120245, DOI: [10.1016/j.apcatb.2021.120245](https://doi.org/10.1016/j.apcatb.2021.120245).
- 39 K. W. Zha, C. Feng, L. P. Han, H. R. Li, T. T. Yan, S. Kuboon, L. Y. Shi and D. S. Zhang, Promotional effects of Fe on manganese oxide octahedral molecular sieves for alkali-resistant catalytic reduction of NO<sub>x</sub>: XAFS and *in situ* DRIFTS study, *Chem. Eng. J.*, 2020, **381**, 122764, DOI: [10.1016/j.cej.2019.122764](https://doi.org/10.1016/j.cej.2019.122764).
- 40 T. Yu, T. Hao, D. Q. Fan, J. Wang, M. Q. Shen and W. Li, Recent NH<sub>3</sub>-SCR Mechanism Research over Cu/SAPO-34 Catalyst, *J. Phys. Chem. C*, 2014, **118**, 6565–6575, DOI: [10.1021/jp4114199](https://doi.org/10.1021/jp4114199).
- 41 S. H. Zhan, H. Zhang, Y. Zhang, Q. Shi, Y. Li and X. J. Li, Efficient NH<sub>3</sub>-SCR removal of NO<sub>x</sub> with highly ordered mesoporous WO<sub>3</sub>(x)-CeO<sub>2</sub> at low temperatures, *Appl. Catal., B*, 2017, **203**, 199–209, DOI: [10.1016/j.apcatb.2016.10.010](https://doi.org/10.1016/j.apcatb.2016.10.010).
- 42 H. Wang, Z. P. Qu, S. C. Dong and C. Tang, Mechanism study of FeW mixed oxides to the selective catalytic reduction of NO with NH<sub>3</sub>: *in situ* DRIFTS and MS, *Catal. Today*, 2018, **307**, 35–40, DOI: [10.1016/j.cattod.2017.05.071](https://doi.org/10.1016/j.cattod.2017.05.071).

